JACS
JOURNAL OF THE AMERICAN CHEMICAL SOCIETY
pubs.acs.org/JACS
Article

Hierarchically Structured Nanocomposites via Mixed-Graft Block Copolymer Templating: Achieving Controlled Nanostructure and Functionality

Yazhen Xue,[‖] Qingliang Song,[‖] Yuchu Liu, Daniel Smith, Weihua Li,* and Mingjiang Zhong*

Cite This: https://doi.org/10.1021/jacs.3c10297

ABSTRACT: Integrating inorganic and polymerized organic functionalities to create composite materials presents an efficient strategy for the discovery and fabrication of multifunctional materials. The characteristics of these composites go beyond a simple sum of individual component properties; they are profoundly influenced by the spatial arrangement of these components and the resulting homo-/hetero-interactions. In this work, we develop a facile and highly adaptable approach for crafting nanostructured polymer−inorganic composites, leveraging hierarchically assembling mixed-graft block copolymers (mGBCPs) as templates. These mGBCPs, composed of diverse polymeric side chains that are covalently tethered with a defined sequence to a linear backbone polymer, self-assemble into ordered hierarchical structures with independently tuned nano- and mesoscale lattice features. Through the coassembly of mGBCPs with diversely sized inorganic fillers such as metal ions (ca. 0.1 nm), metal oxide clusters (0.5−2 nm), and metallic nanoparticles (>2 nm), we create three-dimensional filler arrays with controlled interfiller separation and arrangement. Multiple types of inorganic fillers are simultaneously integrated into the mGBCP matrix by introducing orthogonal interactions between distinct fillers and mGBCP side chains. This results in nanocomposites where each type of filler is selectively segregated into specific nanodomains with matrix-defined orientations. The developed coassembly strategy offers a versatile and scalable pathway for hierarchically structured nanocomposites, unlocking new possibilities for advanced materials in the fields of optoelectronics, sensing, and catalysis.

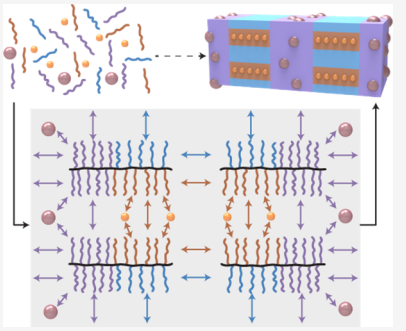

INTRODUCTION

Composite materials, whether artificial[1−4] or natural,[5−7] exploit the synergistic potential that arises from the combination of distinct components to enhance performance and unlock novel functionalities. A notable advancement in this field lies in the integration of functional inorganic motifs into organic polymer matrices, resulting in polymer−inorganic composites that exhibit collective properties surpassing those of their individual constituents.[8−12] These hybrid materials effectively capture the versatile thermomechanical properties and processability inherent in polymeric materials, rendering them highly favorable for industrial device fabrication. Their advanced applications in optoelectronics,[13−17] energy storage,[18−21] and catalysis[17,22,23] benefit substantially from the diverse behaviors exhibited by the inorganic fillers,[24] particularly in relation to charge transfer and energy conversion.[25−27]

Engineering the nanostructures of polymer−inorganic nanocomposites plays a crucial role in achieving desired properties.[28] Integrating inorganic fillers into composite materials with precise spatial arrangements ensures controlled and specific interactions between the fillers and their surrounding polymer matrices, thereby enhancing the material properties. However, traditional high-resolution top-down strategies, such as electron-beam lithography and ion-beam milling, face limitations in scalability and the creation of three-dimensionally ordered nanostructures.[29] In contrast, bottom-up approaches based on the coassembly of inorganic fillers and polymers offer control over the filler distribution within a macroscopic polymer matrix.[28,30−33] Among various strategies explored, coassembly templated by self-assembled block copolymers (BCPs) has emerged as a versatile and scalable approach.[34]

BCPs, composed of covalently linked immiscible homopolymer blocks, undergo a thermodynamically driven phase-separation process, resulting in ordered nanostructures.[35] Coassembling BCPs with interaction-specific inorganic fillers creates nanocomposites featuring periodically arranged polymer nanodomains enriched with the inorganic components.[36−43] Despite significant progress in understanding coassembly mechanisms and identifying suitable BCP inter-

Received: September 19, 2023
Revised: November 30, 2023
Accepted: December 1, 2023

https://doi.org/10.1021/jacs.3c10297
J. Am. Chem. Soc. XXXX, XXX, XXX−XXX

actions with a variety of inorganic fillers, challenges persist in achieving a high degree of precision and flexibility in controlling the distance between individual inorganic objects throughout a three-dimensional space. This can primarily be attributed to the limited scope of morphologies and tuning capabilities of characteristic length scales in conventional linear BCPs, as well as the complex perturbation of added inorganic fillers on the BCP self-assembly behaviors. Additionally, developing BCP-derived nanocomposites that incorporate multiple types of inorganic species with independently controlled spatial arrangements and orientations remains a challenge.

Mixed-graft block copolymers (mGBCPs) present a compelling alternative to traditional BCPs by incorporating two or more dissimilar polymeric side chains covalently attached to a backbone polymer.[44,45] This unique architecture combines the advantageous characteristics of both BCPs and graft polymers, enabling the fabrication of hierarchically structured materials that span from the nanoscale (~1−100 nm) to mesoscale (~100 nm−1 μm) features.[46−48] In our previous work, we synthesized ternary mGBCPs comprising A, B, and C side chains, where A and B side chains were arranged with a pseudoalternating (*-alt-*)[46] or random (*-ran-*)[47] sequence, extended with a homograft block tethered exclusively with C side chains. The immiscibility of A and B side chains in these (A-*alt*/*ran*-B)-*b*-C type mGBCPs resulted in intramolecular phase separation, leading to the formation of substructures within A- and B-rich nanodomains interfaced with the backbone (Figure 1a, yellow planes). The phase separation of the C-containing block with both A and B nanodomains created superstructures with a distinct interface perpendicular to the backbone (Figure 1a, blue planes). The characteristic lengths of the super- and substructures can be independently tuned over a broad range of length scales by adjusting the degrees of polymerization (DPs) of the backbone and A/B side chains, respectively. Consequently, these mGBCPs offer a promising category of template materials for designing nanocomposites with three-dimensionally engineered arrangements of inorganic fillers (Figure 1b). The compositionally diverse nature of mGBCPs also provides a powerful platform for one-pot nanocomposite synthesis. A mixture of multiple fillers can be sorted via orthogonal polymer−filler interactions and separately enriched into distinct nanodomains of mGBCP, paving the way for the development of multifunctional nanomaterials.

In this study, we leveraged the design of mGBCPs to synthesize nanocomposites coassembled from inorganic fillers of varying dimensions, spanning from inorganic ions (ca. 0.1 nm) and clusters (0.5−2 nm) to nanoparticles (2−4 nm) (Figure 1c). Our investigation began with the coassembly of (A-*co*-B)-*b*-C mGBCPs and a single type of inorganic fillers by tuning its specific interaction with one of the three side chains, such as poly(ethylene oxide) (PEO). Small-angle X-ray scattering (SAXS) and transmission electron microscopy (TEM) were employed to confirm that a controlled quantity of fillers could be positioned in the PEO-rich nanodomains, resulting in hierarchically structured nanocomposites with a morphology resembling that of the parent mGBCPs. This nanodomain-specific integration of fillers with minimal impact on the hierarchical morphology of the mGBCP template offers a straightforward methodology for fabricating nanocomposite with predictable overall nanostructures and filler arrangement. The simultaneous incorporation of multiple types of inorganic

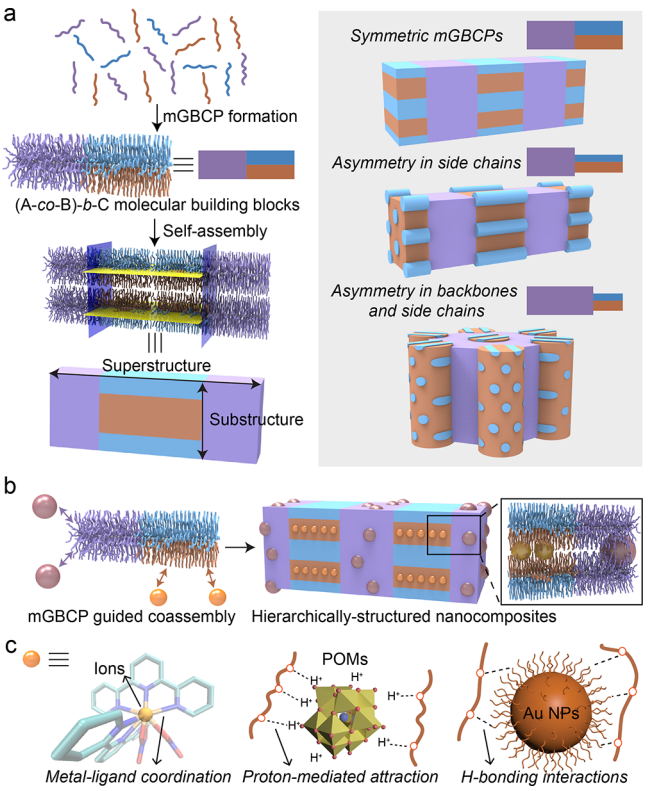

Figure 1. Overview of the mGBCP-templated nanocomposites. (a) Hierarchical assembly of (A-*co*-B)-*b*-C mGBCPs toward nanostructures with perpendicularly oriented super- and substructures and diverse phase-*in*-phase morphologies. (b) One-pot coassembly synthesis of nanocomposites containing distinct inorganic fillers enriched in select nanodomains. (c) Inorganic fillers utilized in this study including photoluminescent metal ions, POMs, and Au NPs.

fillers into dissimilar nanodomains was realized by introducing orthogonal interactions between the fillers and side chains. The use of dissipative particle dynamics (DPD) simulations aids in developing a comprehensive understanding of the molecular structure−morphology relationships observed experimentally, further expanding our scope of mGBCP-based nanocomposite design toward cutting-edge applications.

RESULTS AND DISCUSSION

Design and Synthesis of mGBCPs. The mGBCPs were marked by a general notation, $[(A_x)_m\text{-}co\text{-}(B_y)_n]\text{-}b\text{-}(C_z)_p$, where A, B, and C represent chemical compositions of side chains with a number-average DP of *x*, *y*, and *z*, respectively, while the subscripts *m*, *n*, and *p* quantify the number of A_x, B_y, and C_z side chains attached to the backbones. The synthesis of the mGBCPs was accomplished by the ring-opening metathesis polymerization (ROMP) of *exo*-norbornene (Nb)-based macromonomers initiated by the Grubbs third-generation catalyst (G3)[49] (Figure 2a). Specifically, the $(A_x)_m\text{-}co\text{-}(B_y)_n$ block was synthesized either by the homopolymerization of the Nb-based branched macromonomer (BMM), marked as Nb-(A_x-*branch*-B_y), or by the statistical copolymerization of two Nb-terminated linear macromonomers (LMMs), denoted as Nb-A_x and Nb−B_y, respectively. In this stage, a nearly quantitative conversion of macromonomers was achieved due to the high initiation efficiency and reactivity of G3. This efficient polymerization was followed by a one-pot addition of the Nb−C_z macromonomer. The living chain end preserved by

https://doi.org/10.1021/jacs.3c10297
J. Am. Chem. Soc. XXXX, XXX, XXX−XXX

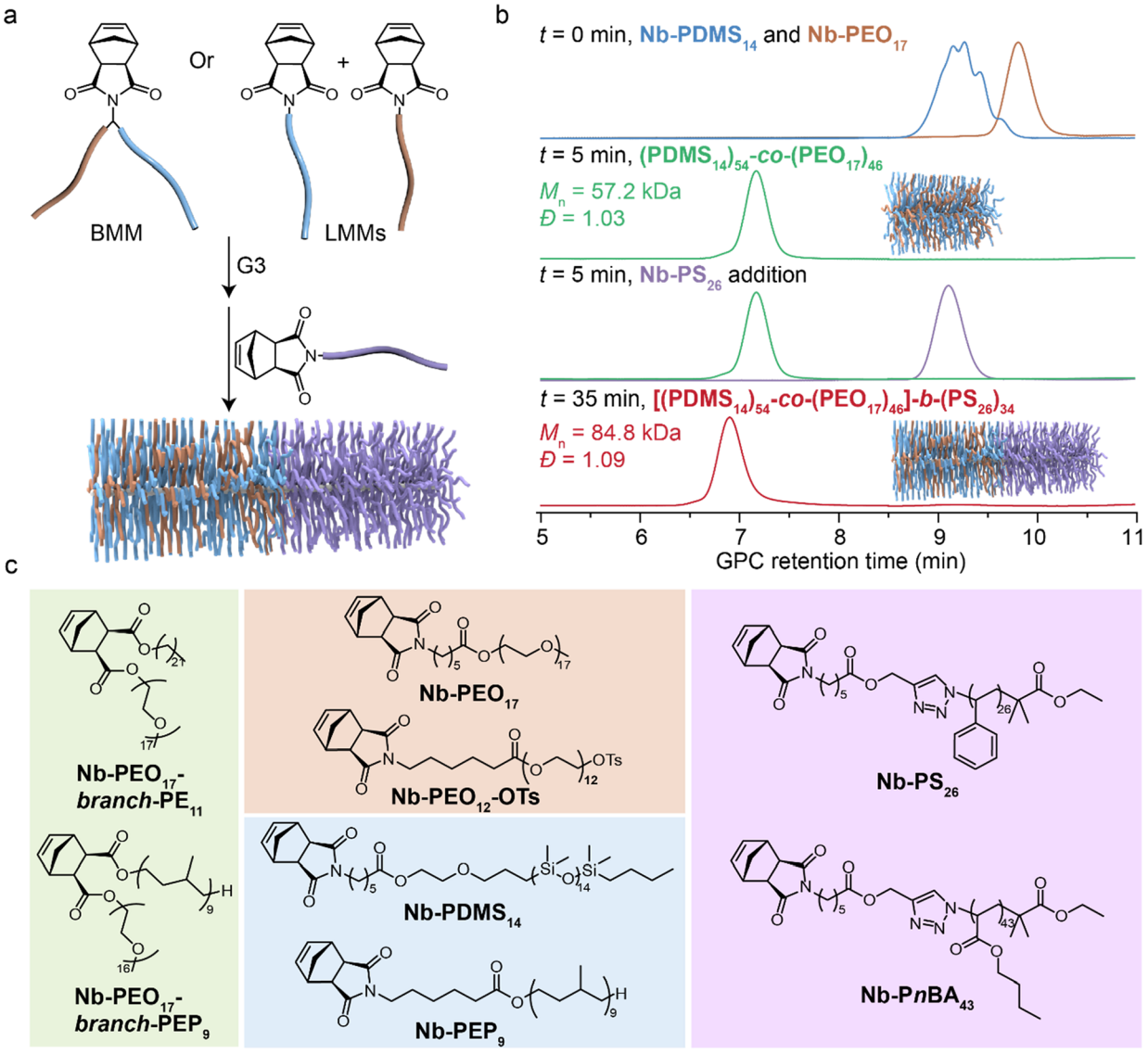

Figure 2. Design and synthesis of the mGBCPs. (a) Synthetic scheme for the preparation of representative (A-*co*-B)-*b*-C-type mGBCPs. Both homopolymerization of Nb-(A-*branch*-B) BMM and copolymerization of Nb-A and Nb−B LMMs were used in the synthesis of (A-*co*-B) macroinitiators. (b) GPC traces corresponding to each synthetic stage during the $[(PDMS_{14})_{54}$-*co*-$(PEO_{17})_{46}]$-*b*-$(PS_{26})_{34}$ mGBCP synthesis. M_n and $Đ$ of $[(PDMS_{14})_{54}$-*co*-$(PEO_{17})_{46}]$ and $[(PDMS_{14})_{54}$-*co*-$(PEO_{17})_{46}]$-*b*-$(PS_{26})_{34}$ were determined by GPC using a linear PS standard. (c) Chemical structures of the macromonomers used for the synthesis of mGBCPs.

the $(A_x)_m$-*co*-$(B_y)_n$ block will continue to grow by polymerizing with Nb−C_z until its full consumption, resulting in the final $[(A_x)_m$-*co*-$(B_y)_n]$-*b*-$(C_z)_p$ mGBCP products. Notably, each element of the structural parameter library [*x, m, y, n, z, and p*] can be independently tuned by varying the macromonomer structures and relevant feeding ratios, except for the case involving ROMP of Nb-$(A_x$-*branch*-$B_y)$, where $m = n$.

Figure 2b illustrates a typical synthetic procedure of mGBCPs incorporating PEO, polydimethylsiloxane (PDMS), and polystyrene (PS) side chains. Nb-$PDMS_{14}$ and Nb-PEO_{17} LMMs were randomly copolymerized at a $[Nb\text{-}PDMS_{14}]_0/[Nb\text{-}PEO_{17}]_0/[G3]_0$ ratio of 54/46/1. The reaction achieved over 99% conversion of both LMMs within 5 min, evidenced by the complete disappearance of LMM traces in gel permeation chromatography (GPC). Subsequently, Nb-PS_{26} LMM was added to the reaction at an equivalent of 34 relative to G3, extending the PDMS/PEO-based binary mGBCP to a ternary mGBCP with PS_{26} tethered as the sole side chains in the second backbone block. The original GPC trace clearly shifted to the shorter retention time region with a low dispersity index ($Đ$) of 1.09, underscoring the high degree of control and livingness attained throughout this one-pot, two-step block copolymerization process.

The same process can be extended to diverse macromonomers. Figure 2c summarizes the BMMs and LMMs utilized in the prototype development of mGBCP-based nanocomposites. The selection of side chain compositions, as elucidated in subsequent systems, took various factors into account such as the thermodynamic propensity for phase separation, specificity of interaction with given inorganic fillers, chemical stability in the presence of inorganic fillers, and their commercial availability or synthetic scalability. In the following discussion, mGBCPs with diversified chemical compositions were synthesized by introducing additional Nb-based macromonomers containing poly(*n*-butyl acrylate) (P*n*BA), polyethylene (PE), and polyethylenepropylene (PEP).

https://doi.org/10.1021/jacs.3c10297
J. Am. Chem. Soc. XXXX, XXX, XXX−XXX

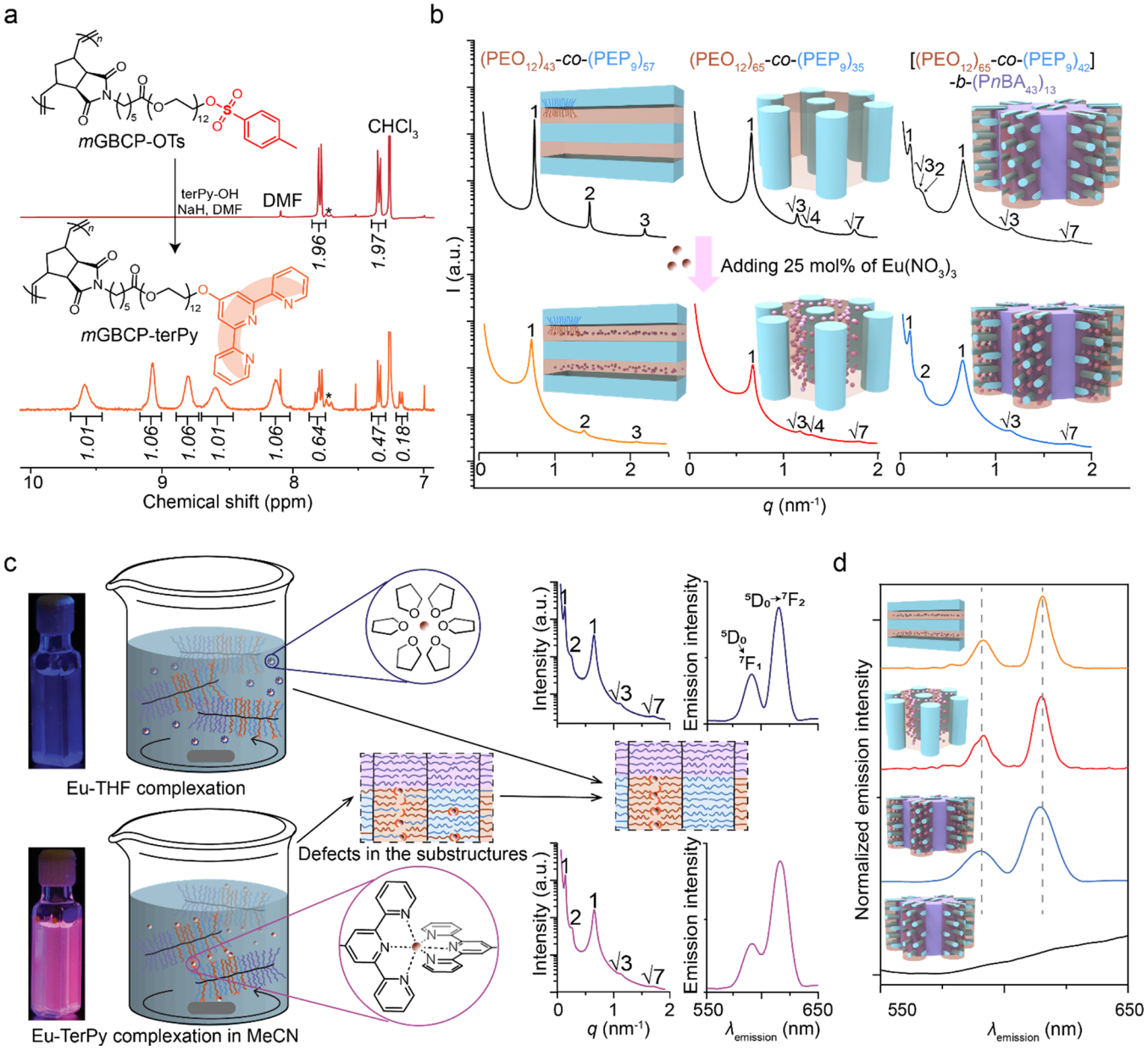

Figure 3. (a) ^{1}H NMR characterization of the PEO side chain end functionalization with terPy groups in $[(PEO_{12})_{65}$-*co*-$(PEP_9)_{42}]$-*b*-$(PnBA_{43})_{13}$ mGBCPs. The integration was based on the proton of the ethylene oxide units. (b) SAXS profiles of three mGBCPs (top) and the corresponding mGBCP/$Eu(NO_3)_3$ composites (bottom). The loading of $Eu(NO_3)_3$ was 25 mol % with respect to the terPy chain ends. (c) Schematic comparison (left) of the solution processing of $Eu(NO_3)_3$ and $[(PEO_{12})_{65}$-*co*-$(PEP_9)_{42}]$-*b*-$(PnBA_{43})_{13}$ mGBCPs using THF and MeCN solvents as well as the SAXS profiles (middle) and fluorescence spectra (right) of the respectively obtained composite films. (d) Comparison of photoluminescence spectra of different composite films containing 25 mol % Eu^{3+}. From top to bottom: $(PEO_{12})_{43}$-*co*-$(PEP_9)_{57}$/$Eu(NO_3)_3$, $(PEO_{12})_{65}$-*co*-$(PEP_9)_{35}$/$Eu(NO_3)_3$, $[(PEO_{12})_{65}$-*co*-$(PEP_9)_{42}]$-*b*-$(PnBA_{43})_{13}$/$Eu(NO_3)_3$, and $[(PEO_{12})_{65}$-*co*-$(PEP_9)_{42}]$-*b*-$(PnBA_{43})_{13}$.

Photoluminescent Nanocomposites Fabricated through Chain End-Ion Complexation. Creating an isolated or noninterfering environment for chromophores, when introduced into composites, is essential for the preservation of their photoluminescent activity.[50] To achieve this, we utilized mGBCP-templated coassembly, which selectively distributed the chromophores into periodically spaced nanodomains within a hierarchical structure. A blending-then-annealing procedure was developed for the large-scale synthesis of photoluminescent nanocomposites. As a proof-of-concept demonstration, we chose photoluminescent trivalent europium (Eu^{3+}) complexes exhibiting long-life red fluorescence[51] to conduct the coassembly studies.

To disperse Eu^{3+} within the mGBCP matrix, we synthesized binary $(PEO_{12})_{43}$-*co*-$(PEP_9)_{57}$ and $(PEO_{12})_{65}$-*co*-$(PEP_9)_{35}$, as well as the ternary $[(PEO_{12})_{65}$-*co*-$(PEP_9)_{42}]$-*b*-$(PnBA_{43})_{13}$ mGBCPs, in which the free ends of PEO side chains were functionalized with toluene-4-sulfonate (−OTs) groups. The −OTs groups originating from the Nb-PEO_{12}−OTs LMM (Figure 2b) were substituted with [2,2′:6′,2″-terpyridine]-4′-ol (terPy) postpolymerization, allowing for the introduction of Eu^{3+}/terPy chromophores within the PEO-rich nanodomains in the coassembled structures. Proton nuclear magnetic resonance (^{1}H NMR) spectroscopic analysis suggested a 50% efficiency of the PEO-chain-end functionalization in $[(PEO_{12})_{65}$-*co*-$(PEP_9)_{42}]$-*b*-$(PnBA_{43})_{13}$ (Figures 3a, S52−55),

https://doi.org/10.1021/jacs.3c10297
J. Am. Chem. Soc. XXXX, XXX, XXX−XXX

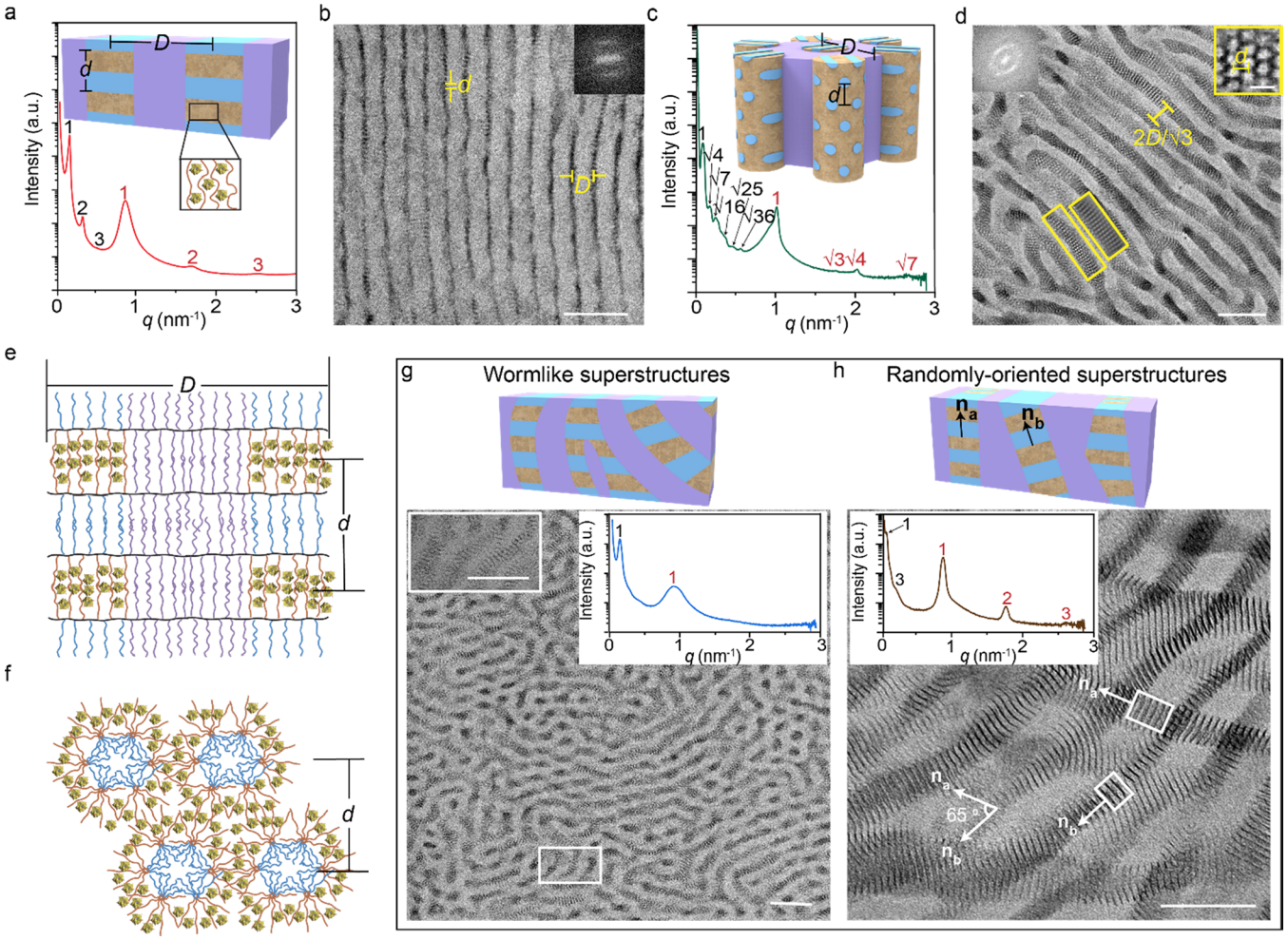

Figure 4. (a) SAXS profiles and (b) TEM image of $[(PEO_{17})_{100}$-*co*-$(PE_{11})_{100}]$-*b*-$(PS_{26})_{32}$/50 wt % PTAs nanocomposites. Inset of (a): schematic illustration of LAM-*in*-LAM with PTAs localized in the sublamellae. (c) SAXS profiles and (d) TEM image of $[(PEO_{17})_{100}$-*co*-$(PE_{11})_{100}]$-*b*-$(PS_{26})_{50}$/150 wt % PTAs nanocomposites. Inset of (c): schematic illustration of HPC-*in*-HPC with PTAs localized in the continuous phase of the subdomain. Schematic representation of the PTA distribution in the (e) LAM and (f) HPC substructures. TEM images and SAXS profiles (white-backgrounded insets) of (g) $[(PEO_{17})_{100}$-*co*-$(PE_{11})_{100}]$-*b*-$(PS_{26})_{32}$/100 wt % PTAs and (h) $[(PEO_{17})_{100}$-*co*-$(PEP_{9})_{100}]$-*b*-$(PS_{26})_{52}$/100 wt % PTAs nanocomposites. Scale bars in (b), (d), (g), and (h): 100 nm. Scale bars in inset of (d): 10 nm. The black and red numbers correspond to the indices of the superstructures and substructures, respectively.

while 62 and 82% reaction efficiencies were achieved in $(PEO_{12})_{43}$-*co*-$(PEP_{9})_{57}$ and $(PEO_{12})_{65}$-*co*-$(PEP_{9})_{35}$, respectively (Figures S48−51).

The solution-based coassembly process was carried out by mixing mGBCPs and $Eu(NO_3)_3$ in either tetrahydrofuran (THF) or acetonitrile (MeCN) of varying chelating strength toward Eu^{3+}. For the sample cast from THF, SAXS characterization indicated that the nanostructures of the three resulting nanocomposites remained consistent with their parent mGBCP morphologies at a 25 mol % Eu^{3+} loading, although the ordering of the nanostructures was compromised upon ion incorporation (Figures 3b and S9). The binary $(PEO_{12})_{43}$-*co*-$(PEP_{9})_{57}$ and $(PEO_{12})_{65}$-*co*-$(PEP_{9})_{35}$ produced lamellae (LAM) and hexagonally packed cylinders (HPC), respectively, whereas the ternary mGBCP yielded HPC-*in*-HPC structures. The hierarchical phase-*in*-phase structure derived from the ternary mGBCP contained an HPC superstructure with a domain spacing of 47.4 nm, formed through the phase separation between P*n*BA and PEO/Eu^{3+}-*co*-PEP, and an HPC substructure with a 9.4 nm domain spacing, containing PEP cylinders that were distributed in a continuous PEO/Eu^{3+} phase.

During the coassembling process, the characteristic red emission of Eu^{3+}/terPy at 250 nm excitation was evident in the MeCN solution due to the weak solvent binding with Eu^{3+} (Figure 3c left, and Figure S11). This early stage formation of Eu^{3+}/terPy, which was suppressed in the strongly coordinating THF solvent, led to inter-mGBCP cross-linking through a 2 + 1 complexation between terPy and Eu^{3+}. This reversible cross-linking hindered the chain rearrangement during the coassembly, resulting in less ordered nanostructures in the under-aged samples (Figures 3c and S10). Nevertheless, owing to the dynamic nature of the coordination bonds and the low degree of chain entanglement due to the graft polymer architecture,[52,53] extending annealing time allowed for the reduction of these kinetically arrested defects. Hierarchical nanostructures with a similar degree of ordering to the samples prepared from the THF solution developed after 1 week of storage of the composite films under ambient conditions (Figure 3c, middle).

https://doi.org/10.1021/jacs.3c10297
J. Am. Chem. Soc. XXXX, XXX, XXX−XXX

We next examined the optical properties of the composite films by using fluorescence spectroscopy. All three films, with chromophores residing in their corresponding PEO phases, displayed the characteristic $^5D_0 \rightarrow {}^7F_1$ and $^5D_0 \rightarrow {}^7F_2$ emissions, as shown in Figure 3d. Remarkably, the emission wavelengths of the composite films deviated by less than 0.3 nm from those of the dilute Eu^{3+}/mGBCP complex solution in MeCN (Figure S11). This minimal discrepancy underscores the homogeneous dispersion of the chromophores in the solid state, mirroring their behaviors in dilute solutions. Additionally, irrespective of processing solvent, composite films cast from MeCN and THF showed consistent absolute emission intensities (Figure 3c right, and Figure S12), further highlighting the reproducibility and robustness of this pathway-independent fabrication method.

Proton-Mediated Assembly of POM Clusters in mGBCPs. Polyoxometalates (POMs) are anionic metal oxide clusters composed of high-valent early transition metals. They are valued for their extensive structural tunability and distinctive properties such as acidity,[54] redox activity,[55] and magnetic properties.[56] However, their applications in catalysis, ion conduction, sensing, and energy conversion often encounter challenges associated with activity loss resulting from aggregation and precipitation under working conditions. While depositing POMs onto various substrates has proven effective,[57,58] introducing them through mGBCP coassembly offers an enhanced level of dispersion control, enabling precise enrichment within specific nanodomains of diverse hierarchical structures.

Herein, we demonstrate the feasibility of our method using phosphotungstic acid ($H_3[PW_{12}O_{40}]$, PTA), a classic Keggin-type POM,[59] in combination with PEO containing mGBCPs. The PEO side chains in the designed mGBCPs, that is, $[(PEO_{17})_{100}$-*co*-$(PE_{11})_{100}]$-*b*-$(PS_{26})_{32}$, $[(PEO_{17})_{100}$-*co*-$(PE_{11})_{100}]$-*b*-$(PS_{26})_{50}$, and $[(PEO_{17})_{100}$-*co*-$(PEP_9)_{100}]$-*b*-$(PS_{26})_{52}$, facilitate attraction between polar ether groups from PEO and protons from POMs,[42,60,61] creating a strong affinity to retain PTAs within PEO nanodomains (Figure 1c, middle). The coassembly process involved dissolving mGBCPs and PTA in DMF, followed by solvent removal under reduced pressure, and finally thermal annealing at 120 °C for 30 min under an inert atmosphere to obtain nanocomposites.

Coassembling $[(PEO_{17})_{100}$-*co*-$(PE_{11})_{100}]$-*b*-$(PS_{26})_{32}$ with 50 wt % PTAs generated an LAM-*in*-LAM structures. Two sets of Bragg peaks both with a q ratio of 1:2:3 appeared in the low- and high-q regions of the SAXS profile (Figure 4a), indicating the formation of two sets of LAMs at distinct scales, and it remained consistent after 5 months of storage under ambient conditions (Figure S16), demonstrating its stability against PTA aggregation. The phase separation between PS and PEO(PTA)-*co*-PE block gave rise to the larger dimension LAM superstructure with a domain spacing D of 41.6 nm, while the phase separation between PEO(PTA) and PE was attributed to the smaller scale LAM substructure with a domain spacing d of 7.3 nm. As confirmed by the TEM imaging, the coassembling process precisely located the PTAs within the PEO subdomains, forming dark short strips with thin-layered arrangement (Figure 4b,e).

Nanocomposites consisting of $[(PEO_{17})_{100}$-*co*-$(PE_{11})_{100}]$-*b*-$(PS_{26})_{50}$ and 150 wt % PTAs formed an HPC-*in*-HPC morphology, as evidenced by a SAXS pattern with red-indexed q ratios of $1:\sqrt{3}:\sqrt{4}:\sqrt{7}$ and black-indexed q ratios of $1:\sqrt{4}:\sqrt{7}:\sqrt{16}:\sqrt{25}:\sqrt{36}$ in Figure 4c.[62−64] The isolated bright nanodomains shown in the TEM image affirmed the hexagonal distribution of PE-rich subcylinders within a continuous PEO(PTA) matrix (Figure 4d,f). At a larger scale, the phase separation between PS and the PEO(PTA)-*co*-PE cylinders resulted in the HCP superstructures. To our knowledge, this unique HPC-*in*-HPC was experimentally visualized for the first time and differed from the CYL-*out*-CYL structures previously reported in the neat (A-*co*-B)-*b*-C mGBCP self-assembly, where the A-cylinders were positioned within the continuous phase of superstructures and aligned either perpendicular to the surface of C-cylinders[46] or radiating outward from each C-cylinder.[65] The addition of PTAs into the PEO domains may render the HPC-*in*-HPC structure in a stable state (Figures S17−18), as detained by the strong interaction between PTA and PEO segments.

In addition to achieving hierarchically structured nanocomposites with ordered POM arrangement at both micro- and mesoscales, mGBCP templating has also demonstrated its robustness by allowing for intentional disordering at one of these two length scales with minimal disruption to the ordering of the other length scale. A PTA loading of 100 wt % within $[(PEO_{17})_{100}$-*co*-$(PE_{11})_{100}]$-*b*-$(PS_{26})_{32}$ induced curvature in the LAM superstructures,[66] resulting in a SAXS pattern displaying a broad reflection peak and TEM images featured with mixed worm-like layers and dotted objects (Figures 4g, S20). This observed disordered superstructure hosted locally ordered PTA layers with a thickness of 3.0 nm, similar to the PTA layers (2.7 nm) embedded in the LAM-*in*-LAM structures (see the detailed calculation for PTA layer thickness in Table S3 and Figure S22). Similarly, when using $[(PEO_{17})_{100}$-*co*-$(PEP_9)_{100}]$-*b*-$(PS_{26})_{52}$ as templates and introducing 100 wt % PTAs, a lamellar substructure with PTA layers measuring 2.4 nm thick and a less ordered lamellar superstructure were obtained (Figure 4h). To assess the superstructure heterogeneity, we grouped neighboring PEO(PTA) layers oriented in the same direction, as illustrated by the white-framed areas in Figure 4h. By calculating the angles between the normal vectors ($\mathbf{n}$) of different groups, we semiquantitively evaluated the degree of ordering of superstructures across various sections. For instance, the angle of 65° between the two PTA groups highlighted in Figure 4h ($\mathbf{n}_a$ and $\mathbf{n}_b$) was markedly larger than that of the LAM-*in*-LAM shown in Figure 4b with angles consistently below 15° (Figure S23), suggesting a more randomized orientation of superstructure domains in Figure 4h.

Hierarchically Assembled NP Arrays. Assembling plasmonic nanoparticles (NPs), typically sized from a few to tens of nanometers, into three-dimensionally ordered arrays not only is an effective way to enhance or tune their localized surface plasmon resonance activities[67−69] but also provides a material platform for harnessing this phenomenon in sensing,[70] photonic crystals,[71] and surface-enhanced Raman scattering.[72−74] Here, we employ mGBCPs to template the NP assembly, aiming at addressing two challenges remaining in the fabrication of three-dimensional NP arrays. First, we aim to synthesize NP arrays with independently tunable interparticle distances between adjacent NPs along different orientations. As a model example, 4-mercaptophenol functionalized gold NPs with a diameter (d_{NP}) of 2.0 nm were prepared (see Scheme S12 for synthesis)[75] and mixed with $[(PEO_{17})_{46}$-*co*-$(PDMS_{14})_{54}]$-*b*-$(PS_{26})_{34}$ in DMF solution. After the solvent removal and sample annealing, the coassembly afforded

https://doi.org/10.1021/jacs.3c10297
J. Am. Chem. Soc. XXXX, XXX, XXX−XXX

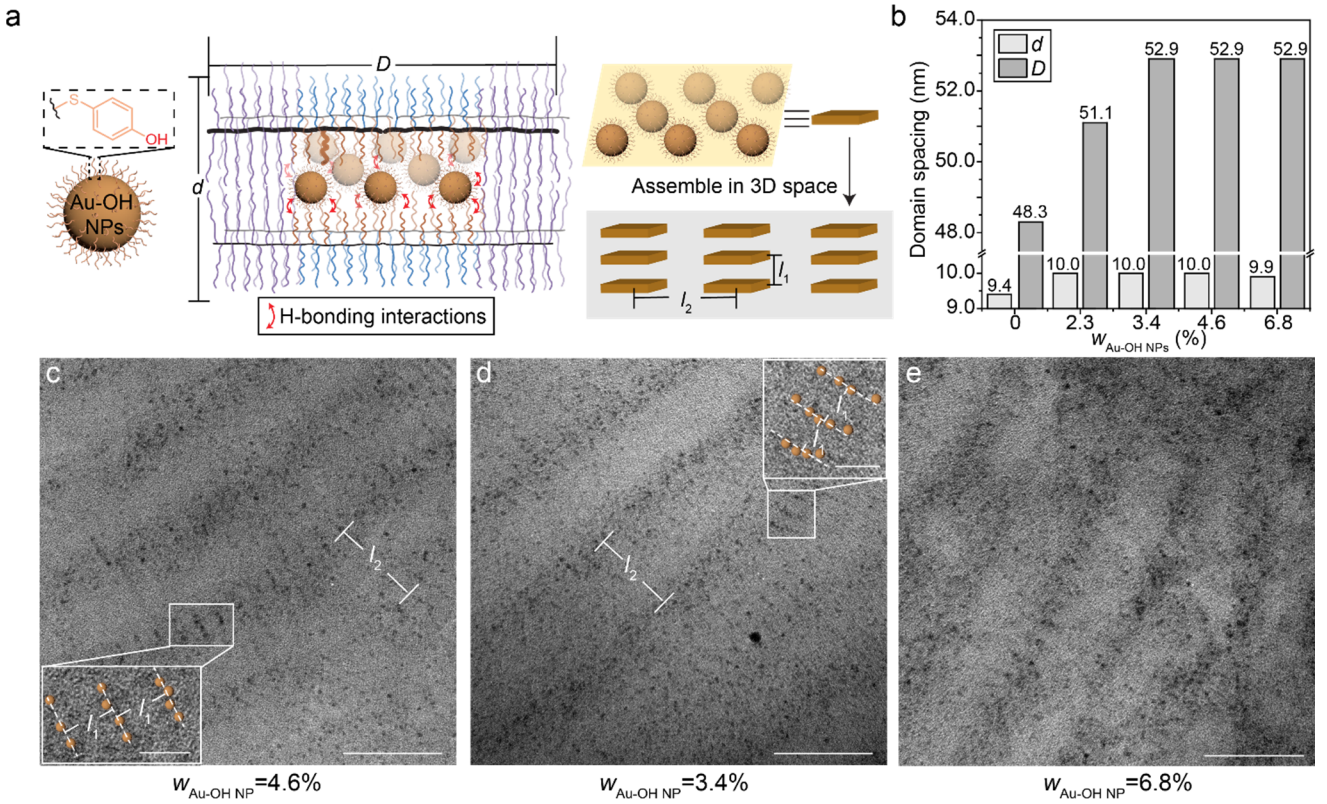

Figure 5. (a) Schematic representation of the coassembled structure of $[(PEO_{17})_{46}$-*co*-$(PDMS_{14})_{54}]$-*b*-$(PS_{26})_{34}$ mGBCPs/Au−OH NP nanocomposites, where the backbone extension and PEO side chain (brown) compression were highlighted. The hierarchically arranged NP arrays with l_1 and l_2 indicated was provided on the right. (b) Summary of the super- and substructure domain sizes of $[(PEO_{17})_{46}$-*co*-$(PDMS_{14})_{54}]$-*b*-$(PS_{26})_{34}$/Au−OH NPs with 0, 2.3, 3.4, 4.6, and 6.8 wt % of Au−OH NPs. TEM images showing the inclusion of Au−OH NPs at (c) 4.6 wt %, (d) 3.4 wt %, and (e) 6.8 wt % NP loading. Scale bar: 50 nm. Inset: zoomed-in images of the substructures with embedded NPs. Scale bar: 10 nm.

nanocomposites with LAM-*in*-LAM structures in which quasi-two-dimensional NP arrays are periodically stacked along the third dimension (Figures 5a and S28). The hydroxyl-functionalized inorganic fillers, termed Au−OH NPs, mediate hydrogen bonding interactions between the PEO side chains and NP surfaces, leading to the residence of NPs within PEO domains. The characteristic lengths of quasi-two-dimensional NP arrays sandwiched between two adjacently stacked mGBCPs are infinitely extended at one side and are defined at the other side by the mGBCP backbone length. At an NP loading of 4.6 wt %, the thickness of the quasi-two-dimensional array was measured as 2.2 nm using high-resolution TEM. This measurement is comparable to d_{NP}, suggesting the formation of NP monolayers (Figure 5c). The emergence of this monolayer was possibly due to the densely grafted side chains in the mGBCPs, which predominantly permitted NPs to localize around the side chain ends and therefore avoided the larger entropic penalty when the NPs were moving closer to the backbones. DPD simulations also suggested a favorable interaction between the NPs and the more accessible PEO chain ends (Figure S30). Regulated by the compositionally anisotropic mGBCP templates, NP assemblies were arranged into an ordered array that was defined by two distances within the LAM-*in*-LAM matrix, l_1 and l_2 (Figure 5a), which were determined by the lattice parameters of the molecular templates D and d, respectively. A measurement of l_1 (46.9 nm) and l_2 (10.7 nm) taken from Figure 5c was consistent with the domain sizes calculated from the SAXS results (Figure 5b).

The LAM-*in*-LAM structure was retained with NP loadings from 0 to 4.6 wt % (Figures 5d and S28). However, increasing NP loading to 6.8 wt % oversaturated the PEO nanodomains, consequently disrupting both super- and substructures due to NP agglomeration (Figure 5e). Unlike the high capacity of subnanometer-scale PTAs within the PEO domains, the localization of more NPs with larger sizes in the interstitial sites requires additional compression of PEO chains within the quasi-two-dimensional confined subdomains and reduces both the translational entropy of NPs and conformational entropy of the side chains.[76−79] This process is thermodynamically unfavorable and ultimately leads to structural disordering.

The modular surface functionalities of Au NPs enable their integration into various domains beyond PEO, providing a solution to another challenge in polymer−NP nanocomposite fabrication: the controlled and independent integration of more than one type of NPs into the polymer matrix. In this study, we synthesized PS-functionalized hairy gold NPs (Au−PS NPs) with a 3.1 nm core diameter (see Scheme S13 for synthesis). We blended $[(PEO_{17})_{100}$-*co*-$(PE_{11})_{100}]$-*b*-$(PS_{26})_{50}$ mGBCP simultaneously with Au−PS NPs and PTAs, which provided specific interaction with PS and PEO side chains, respectively, via van der Waals interactions and proton-mediated attraction (Figure 6a). The dispersion of both inorganic fillers was confirmed by TEM imaging (Figure 6b) and DPD simulation (Figure S34). The dark dotted objects, matching in size (Figure 6c) with the neat Au−PS NPs (Figure S31), were evenly distributed in the bright PS domains. When the loading of Au−PS NPs was increased from 15 to 50 wt %

https://doi.org/10.1021/jacs.3c10297
J. Am. Chem. Soc. XXXX, XXX, XXX−XXX

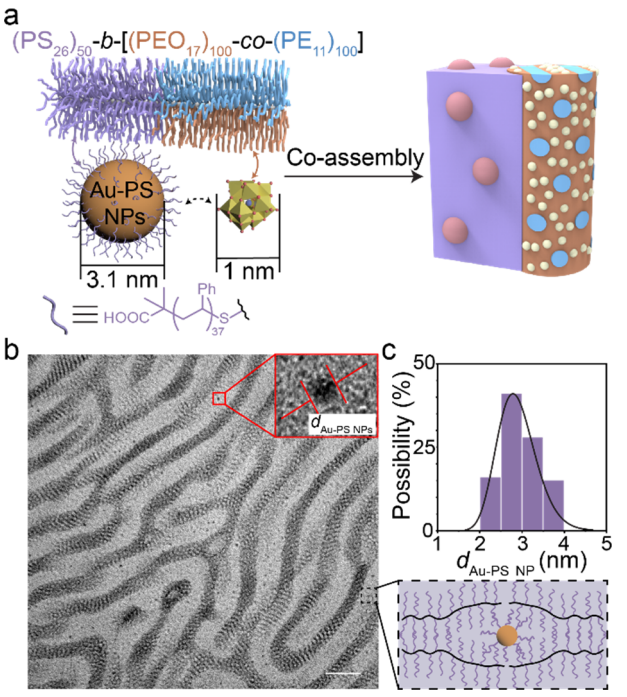

Figure 6. (a) Schematic representation of the mGBCPs, Au−PS NPs, PTAs, and their coassembled nanocomposites. (b) TEM image of the coassembled nanocomposites at 15 wt % Au−PS NP and 150 wt % PTA loading. Scale bar: 50 nm. A schematic representation of the domain expansion upon Au−PS NP incorporation is provided at the right side of the TEM image. (c) Statistics of particle diameters of Au−PS NP embedded in the PS domains.

(Figure S32), the TEM images displayed an expanded area of the bright domain containing the NPs. In both cases, PTAs resided in the PEO subdomains with an HPC morphology, as evidenced by the hexagonally patterned bright PE cylinders. This configuration was consistent with Figure 4d, further demonstrating the independent tunability of individual domains and the structural stability of the nanocomposites. This mGBCP coassembly with multiple fillers, achieved through orthogonal polymer−inorganic interactions, holds promise for the creation of multifunctional composite materials where the location and orientation of different fillers can be precisely engineered.

CONCLUSIONS

In this study, we have introduced a facile approach to coassembling polymers and inorganic materials to synthesize hierarchically structured nanocomposites. This coassembly technique involves the precise synthesis of mGBCP templates and the engineering of polymer−inorganic filler interactions. The inorganic fillers, including europium ions, POM clusters, and surface-functionalized Au NPs, interacted with specific mGBCP side chains through intermolecular forces like metal−ligand coordination, proton-mediated attraction, hydrogen bonding, and van der Waals interactions. Through this molecular coassembly strategy, we achieved precise confinement of the inorganic fillers within select subdomains of the hierarchical nanostructures. We successfully obtained three-dimensional assemblies with controlled interfiller distances and diverse phase-*in*-phase nanomorphologies. Two distinct types of inorganic fillers were separately enriched into different nanodomains in an mGBCP matrix through orthogonally recognized filler−polymer interactions. This innovative hierarchical coassembly methodology provides an ideal model for systematically investigating particle−particle and particle−environment interactions as well as their impact on the ensemble properties in nanostructured organic−inorganic hybrid materials. These advancements will also facilitate the discovery and design of next-generation composite materials integrated with multiple independently tuned functions.

ASSOCIATED CONTENT

Supporting Information

The Supporting Information is available free of charge at https://pubs.acs.org/doi/10.1021/jacs.3c10297.

Synthetic schemes and purification procedures of LMMs, BMMs, mGBCPs, and nanoparticles; characterization data of all samples including GPC, NMR, fluorescence, SAXS, TEM, and DPD simulation; summary of widths and areas of the emission peaks in fluorescence spectra; summary of PTA layer thicknesses; summary of sample morphologies and domain spacings; and supporting references (PDF)

AUTHOR INFORMATION

Corresponding Authors

Weihua Li − *State Key Laboratory of Molecular Engineering of Polymers, Key Laboratory of Computational Physical Sciences, Department of Macromolecular Science, Fudan University, Shanghai 200433, China;* orcid.org/0000-0002-5133-0267; Email: weihuali@fudan.edu.cn

Mingjiang Zhong − *Department of Chemical and Environmental Engineering and Department of Chemistry, Yale University, New Haven, Connecticut 06520, United States;* orcid.org/0000-0001-7533-4708; Email: mingjiang.zhong@yale.edu

Authors

Yazhen Xue − *Department of Chemical and Environmental Engineering, Yale University, New Haven, Connecticut 06520, United States;* orcid.org/0000-0002-1696-9575

Qingliang Song − *State Key Laboratory of Molecular Engineering of Polymers, Key Laboratory of Computational Physical Sciences, Department of Macromolecular Science, Fudan University, Shanghai 200433, China*

Yuchu Liu − *Department of Chemical and Environmental Engineering, Yale University, New Haven, Connecticut 06520, United States*

Daniel Smith − *Department of Chemical and Environmental Engineering, Yale University, New Haven, Connecticut 06520, United States;* orcid.org/0009-0006-3835-7816

Complete contact information is available at: https://pubs.acs.org/10.1021/jacs.3c10297

Author Contributions

[‖]Y.X. and Q.S. contributed equally.

Notes

The authors declare no competing financial interest.

ACKNOWLEDGMENTS

This project was financially supported by United States National Science Foundation (DMR-2003875 and DMR-2320956). W.L. thanks support from the National Natural Science Foundation of China (NSFC; 22333002). Q.S. thanks

support from the National Natural Science Foundation of China (NSFC; 22303017). The research used resources of the CMS 11-BM beamline of the National Synchrotron Light Source II, a US Department of Energy Office of Science User Facility operated for the US Department of Energy Office of Science by Brookhaven National Laboratory under contract no. DE-SC0012704, and beamline 12-ID-B of the Advanced Photon Source, a U.S. DOE Office of Science User Facility operated for the DOE Office of Science by Argonne National Laboratory (Contract No. DE-AC02-06CH11357). The authors thank Mr. Z. Jiao for help with figure drawing. The authors are grateful to Dr. R. Li (Brookhaven National Laboratory), Dr. X. Zuo (Argonne National Laboratory), and Dr. B. Q. Mercado (Yale) for their technical assistance with SAXS measurements.

REFERENCES

(1) Mohamed, C.; Jalal El, B.; Issam, H.; Francisco Mata, C.; Guido Di, B., Composite Materials: A Review of Polymer and Metal Matrix Composites, Their Mechanical Characterization, and Mechanical Properties. In *Next Generation Fiber-Reinforced Composites*, Longbiao, L.; António, B. P.; Alexandre, L. P., Eds.; IntechOpen: Rijeka, 2023; p Ch. 2.

(2) Ortiz, C.; Boyce, M. C. Bioinspired structural materials. *Science* **2008**, *319*, 1053−1054.

(3) Studart, A. R. Towards high-performance bioinspired composites. *Adv. Mater.* **2012**, *24*, 5024−5044.

(4) Wegst, U. G.; Bai, H.; Saiz, E.; Tomsia, A. P.; Ritchie, R. O. Bioinspired structural materials. *Nat. Mater.* **2015**, *14*, 23−36.

(5) Dunlop, J. W.; Fratzl, P. Biological composites. *Annu. Rev. Mater. Res.* **2010**, *40*, 1−24.

(6) Eder, M.; Amini, S.; Fratzl, P. Biological composites—complex structures for functional diversity. *Science* **2018**, *362*, 543−547.

(7) Meyers, M. A.; Lin, A. Y.; Seki, Y.; Chen, P.-Y.; Kad, B. K.; Bodde, S. Structural biological composites: an overview. *JOM* **2006**, *58*, 35−41.

(8) Khan, A. U.; Zeltzer, G.; Speyer, G.; Croft, Z. L.; Guo, Y.; Nagar, Y.; Artel, V.; Levi, A.; Stern, C.; Naveh, D. Mutually Reinforced Polymer−Graphene Bilayer Membranes for Energy-Efficient Acoustic Transduction. *Adv. Mater.* **2021**, *33*, No. 2004053.

(9) Podsiadlo, P.; Shim, B. S.; Kotov, N. A. Polymer/clay and polymer/carbon nanotube hybrid organic−inorganic multilayered composites made by sequential layering of nanometer scale films. *Coord. Chem. Rev.* **2009**, *253*, 2835−2851.

(10) Ren, Z.; Yang, J.; Qi, D.; Sonar, P.; Liu, L.; Lou, Z.; Shen, G.; Wei, Z. Flexible sensors based on organic−inorganic hybrid materials. *Adv. Mater. Technol.* **2021**, *6*, No. 2000889.

(11) Zhao, N.; Yan, L.; Zhao, X.; Chen, X.; Li, A.; Zheng, D.; Zhou, X.; Dai, X.; Xu, F.-J. Versatile types of organic/inorganic nanohybrids: from strategic design to biomedical applications. *Chem. Rev.* **2019**, *119*, 1666−1762.

(12) Zhu, Q.-L.; Xu, Q. Metal−organic framework composites. *Chem. Soc. Rev.* **2014**, *43*, 5468−5512.

(13) Benas, J.-S.; Liang, F.-C.; Chen, W.-C.; Hung, C.-W.; Chen, J.-Y.; Zhou, Y.; Han, S.-T.; Borsali, R.; Kuo, C.-C. Lewis adduct approach for self-assembled block copolymer perovskite quantum dots composite toward optoelectronic application: Challenges and prospects. *Chem. Eng. J.* **2022**, *431*, No. 133701.

(14) Hsu, S.-W.; Rodarte, A. L.; Som, M.; Arya, G.; Tao, A. R. Colloidal plasmonic nanocomposites: from fabrication to optical function. *Chem. Rev.* **2018**, *118*, 3100−3120.

(15) Khan, A. U.; Guo, Y.; Chen, X.; Liu, G. Spectral-selective plasmonic polymer nanocomposites across the visible and near-infrared. *ACS Nano* **2019**, *13*, 4255−4266.

(16) Ko, J.; Berger, R.; Lee, H.; Yoon, H.; Cho, J.; Char, K. Electronic effects of nano-confinement in functional organic and inorganic materials for optoelectronics. *Chem. Soc. Rev.* **2021**, *50*, 3585−3628.

(17) Wei, Z.; Duan, H.; Weng, G.; He, J. Metals in polymers: hybridization enables new functions. *J. Mater. Chem. C* **2020**, *8*, 15956−15980.

(18) Lin, Z.; Zeng, Z.; Gui, X.; Tang, Z.; Zou, M.; Cao, A. Carbon nanotube sponges, aerogels, and hierarchical composites: synthesis, properties, and energy applications. *Adv. Energy Mater.* **2016**, *6*, No. 1600554.

(19) Srivastava, S.; Schaefer, J. L.; Yang, Z.; Tu, Z.; Archer, L. A. 25th anniversary article: polymer−particle composites: phase stability and applications in electrochemical energy storage. *Adv. Mater.* **2014**, *26*, 201−234.

(20) Wang, Q.; Zhu, L. Polymer nanocomposites for electrical energy storage. *J. Polym. Sci., Part B: Polym. Phys.* **2011**, *49*, 1421−1429.

(21) Wu, H.; Zhuo, F.; Qiao, H.; Kodumudi Venkataraman, L.; Zheng, M.; Wang, S.; Huang, H.; Li, B.; Mao, X.; Zhang, Q. Polymer-/ceramic-based dielectric composites for energy storage and conversion. *Energy Environ. Sci.* **2022**, *5*, 486−514.

(22) Chen, L.; Xu, Q. Metal-organic framework composites for catalysis. *Matter* **2019**, *1*, 57−89.

(23) Liu, Q.; Wang, X. Cluster-assembled materials: Ordered structures with advanced properties. *InfoMat* **2021**, *3*, 854−868.

(24) Heuer-Jungemann, A.; Feliu, N.; Bakaimi, I.; Hamaly, M.; Alkilany, A.; Chakraborty, I.; Masood, A.; Casula, M. F.; Kostopoulou, A.; Oh, E. The role of ligands in the chemical synthesis and applications of inorganic nanoparticles. *Chem. Rev.* **2019**, *119*, 4819−4880.

(25) Gu, J.; Liu, X.; Lin, E.-C.; Lee, Y.-H.; Forrest, S. R.; Menon, V. M. Dipole-aligned energy transfer between excitons in two-dimensional transition metal dichalcogenide and organic semiconductor. *ACS Photonics* **2018**, *5*, 100−104.

(26) Guzelturk, B.; Demir, H. V. Organic−inorganic composites of semiconductor nanocrystals for efficient excitonics. *J. Phys. Chem. Lett.* **2015**, *6*, 2206−2215.

(27) Renshaw, C. K.; Forrest, S. R. Excited state and charge dynamics of hybrid organic/inorganic heterojunctions. *I. Theory. Phys. Rev. B* **2014**, *90*, No. 045302.

(28) Yi, C.; Yang, Y.; Liu, B.; He, J.; Nie, Z. Polymer-guided assembly of inorganic nanoparticles. *Chem. Soc. Rev.* **2020**, *49*, 465−508.

(29) Jiang, L.; Chen, X.; Lu, N.; Chi, L. Spatially Confined Assembly of Nanoparticles. *Acc. Chem. Res.* **2014**, *47*, 3009−3017.

(30) Hui, C. M.; Pietrasik, J.; Schmitt, M.; Mahoney, C.; Choi, J.; Bockstaller, M. R.; Matyjaszewski, K. Surface-initiated polymerization as an enabling tool for multifunctional (nano-) engineered hybrid materials. *Chem. Mater.* **2014**, *26*, 745−762.

(31) Jones, M. R.; Osberg, K. D.; Macfarlane, R. J.; Langille, M. R.; Mirkin, C. A. Templated techniques for the synthesis and assembly of plasmonic nanostructures. *Chem. Rev.* **2011**, *111*, 3736−3827.

(32) Macfarlane, R. J.; O'Brien, M. N.; Petrosko, S. H.; Mirkin, C. A. Nucleic acid-modified nanostructures as programmable atom equivalents: forging a new "table of elements. *Angew. Chem., Int. Ed.* **2013**, *52*, 5688−5698.

(33) Raee, E.; Yang, Y.; Liu, T. Supramolecular structures based on metal-organic cages. *Giant* **2021**, *5*, No. 100050.

(34) Bockstaller, M. R.; Mickiewicz, R. A.; Thomas, E. L. Block copolymer nanocomposites: perspectives for tailored functional materials. *Adv. Mater.* **2005**, *17*, 1331−1349.

(35) Bates, F. S.; Fredrickson, G. H. Block copolymers—designer soft materials. *Phys. Today* **1999**, *52*, 32−38.

(36) Bockstaller, M. R.; Lapetnikov, Y.; Margel, S.; Thomas, E. L. Size-Selective Organization of Enthalpic Compatibilized Nanocrystals in Ternary Block Copolymer/Particle Mixtures. *J. Am. Chem. Soc.* **2003**, *125*, 5276−5277.

(37) Deshmukh, R. D.; Liu, Y.; Composto, R. J. Two-Dimensional Confinement of Nanorods in Block Copolymer Domains. *Nano Lett.* **2007**, *7*, 3662−3668.

https://doi.org/10.1021/jacs.3c10297
J. Am. Chem. Soc. XXXX, XXX, XXX−XXX

(38) Lin, Y.; Daga, V. K.; Anderson, E. R.; Gido, S. P.; Watkins, J. J. Nanoparticle-Driven Assembly of Block Copolymers: A Simple Route to Ordered Hybrid Materials. *J. Am. Chem. Soc.* **2011**, *133*, 6513−6516.
(39) Ma, L.; Huang, H.; Ercius, P.; Alexander-Katz, A.; Xu, T. Symmetry-Breaking and Self-Sorting in Block Copolymer-Based Multicomponent Nanocomposites. *ACS Nano* **2022**, *16*, 9368−9377.
(40) Pang, X.; He, Y.; Jung, J.; Lin, Z. 1D nanocrystals with precisely controlled dimensions, compositions, and architectures. *Science* **2016**, *353*, 1268−1272.
(41) Wang, Y.; Zhong, M.; Park, J. V.; Zhukhovitskiy, A. V.; Shi, W.; Johnson, J. A. Block co-polyMOCs by stepwise self-assembly. *J. Am. Chem. Soc.* **2016**, *138*, 10708−10715.
(42) Yin, P.; Li, D.; Liu, T. Solution behaviors and self-assembly of polyoxometalates as models of macroions and amphiphilic polyoxometalate−organic hybrids as novel surfactants. *Chem. Soc. Rev.* **2012**, *41*, 7368−7383.
(43) Zhao, Y.; Thorkelsson, K.; Mastroianni, A. J.; Schilling, T.; Luther, J. M.; Rancatore, B. J.; Matsunaga, K.; Jinnai, H.; Wu, Y.; Poulsen, D.; Fréchet, J. M. J.; Paul Alivisatos, A.; Xu, T. Small-molecule-directed nanoparticle assembly towards stimuli-responsive nanocomposites. *Nat. Mater.* **2009**, *8*, 979−985.
(44) Le, A. N.; Liang, R.; Ji, X.; Fu, X.; Zhong, M. Random copolymerization of macromonomers as a versatile strategy to synthesize mixed-graft block copolymers. *J. Polym. Sci.* **2021**, *59*, 2571−2580.
(45) Le, A. N.; Liang, R.; Zhong, M. Synthesis and Self-Assembly of Mixed-Graft Block Copolymers. *Chem.—Eur. J.* **2019**, *25*, 8177−8189.
(46) Liang, R.; Xue, Y.; Fu, X.; Le, A. N.; Song, Q.; Qiang, Y.; Xie, Q.; Dong, R.; Sun, Z.; Osuji, C. O.; Johnson, J. A.; Li, W.; Zhong, M. Hierarchically engineered nanostructures from compositionally anisotropic molecular building blocks. *Nat. Mater.* **2022**, *21*, 1434−1440.
(47) Liang, R.; Song, Q.; Li, R.; Le, A. N.; Fu, X.; Xue, Y.; Ji, X.; Li, W.; Zhong, M. Rapid Access to Diverse Multicomponent Hierarchical Nanostructures from Mixed-Graft Block Copolymers. *Angew. Chem., Int. Ed.* **2022**, *61*, No. e202210067.
(48) Sun, Z.; Liu, R.; Su, T.; Huang, H.; Kawamoto, K.; Liang, R.; Liu, B.; Zhong, M.; Alexander-Katz, A.; Ross, C. A. Emergence of layered nanoscale mesh networks through intrinsic molecular confinement self-assembly. *Nat. Nanotechnol.* **2023**, *18*, 273−280.
(49) Sanford, M. S.; Love, J. A.; Grubbs, R. H. A versatile precursor for the synthesis of new ruthenium olefin metathesis catalysts. *Organometallics* **2001**, *20*, 5314−5318.
(50) Ye, W.; Ma, H.; Shi, H.; Wang, H.; Lv, A.; Bian, L.; Zhang, M.; Ma, C.; Ling, K.; Gu, M. Confining isolated chromophores for highly efficient blue phosphorescence. *Nat. Mater.* **2021**, *20*, 1539−1544.
(51) Bünzli, J.-C. G.; Piguet, C. Taking advantage of luminescent lanthanide ions. *Chem. Soc. Rev.* **2005**, *34*, 1048−1077.
(52) Liang, H.; Cao, Z.; Wang, Z.; Sheiko, S. S.; Dobrynin, A. V. Combs and Bottlebrushes in a Melt. *Macromolecules* **2017**, *50*, 3430−3437.
(53) Liang, H.; Grest, G. S.; Dobrynin, A. V. Brush-like polymers and entanglements: from linear chains to filaments. *ACS Macro Lett.* **2019**, *8*, 1328−1333.
(54) Zhai, L.; Li, H. Polyoxometalate−Polymer hybrid materials as proton exchange membranes for fuel cell applications. *Molecules* **2019**, *24*, 3425.
(55) Horn, M. R.; Singh, A.; Alomari, S.; Goberna-Ferrón, S.; Benages-Vilau, R.; Chodankar, N.; Motta, N.; Ostrikov, K. K.; MacLeod, J.; Sonar, P. Polyoxometalates (POMs): from electroactive clusters to energy materials. *Energy Environ. Sci.* **2021**, *14*, 1652−1700.
(56) Boskovic, C. Rare earth polyoxometalates. *Acc. Chem. Res.* **2017**, *50*, 2205−2214.
(57) Cherevan, A. S.; Nandan, S. P.; Roger, I.; Liu, R.; Streb, C.; Eder, D. Polyoxometalates on functional substrates: concepts, synergies, and future perspectives. *Adv. Sci.* **2020**, *7*, No. 1903511.
(58) Guo, L.; He, L.; Zhuang, Q.; Li, B.; Wang, C.; Lv, Y.; Chu, J.; Song, Y. F. Recent Advances in Confining Polyoxometalates and the Applications. *Small* **2023**, *19*, No. 2207315.
(59) Gumerova, N. I.; Rompel, A. Synthesis, structures and applications of electron-rich polyoxometalates. *Nat. Rev. Chem.* **2018**, *2*, No. 0112.
(60) Liu, G.; Liu, T. Strong attraction among the fully hydrophilic $\{Mo_{72}Fe_{30}\}$ macroanions. *J. Am. Chem. Soc.* **2005**, *127*, 6942−6943.
(61) Liu, Z.; Liu, T.; Tsige, M. Elucidating the origin of the attractive force among hydrophilic macroions. *Sci. Rep.* **2016**, *6*, 26595.
(62) Fukuhara, J.; Yasui, A.; Yamamoto, K.; Sakurai, S. Versatile Controls of Microdomain Morphologies and Temperature Dependencies in Lamellar Spacing by Blending Diblock Copolymers Bearing Antisymmetric Compositions. *ACS omega* **2017**, *2*, 8580−8590.
(63) Hashimoto, T.; Kawamura, T.; Harada, M.; Tanaka, H. Small-angle scattering from hexagonally packed cylindrical particles with paracrystalline distortion. *Macromolecules* **1994**, *27*, 3063−3072.
(64) May, A. W.; Shi, Z.; Wijayasekara, D. B.; Gin, D. L.; Bailey, T. S. Self-assembly of highly asymmetric, poly (ionic liquid)-rich diblock copolymers and the effects of simple structural modification on phase behaviour. *Polym. Chem.* **2019**, *10*, 751−765.
(65) Song, Q.; Dong, Q.; Liang, R.; Xue, Y.; Zhong, M.; Li, W. Hierarchical Self-Assembly of ABC-Type Bottlebrush Copolymers. *Macromolecules* **2023**, *56*, 5470−5481.
(66) Zhang, L.; Cui, T.; Cao, X.; Zhao, C.; Chen, Q.; Wu, L.; Li, H. Inorganic-Macroion-Induced Formation of Bicontinuous Block Copolymer Nanocomposites with Enhanced Conductivity and Modulus. *Angew. Chem., Int. Ed.* **2017**, *56*, 9013−9017.
(67) Bian, K.; Schunk, H.; Ye, D.; Hwang, A.; Luk, T. S.; Li, R.; Wang, Z.; Fan, H. Formation of self-assembled gold nanoparticle supercrystals with facet-dependent surface plasmonic coupling. *Nat. Commun.* **2018**, *9*, 2365.
(68) Duan, H.; Yang, Y.; Zhang, Y.; Yi, C.; Nie, Z.; He, J. What is next in polymer-grafted plasmonic nanoparticles? *Giant* **2020**, *4*, No. 100033.
(69) Li, B.; Wen, X.; Li, R.; Wang, Z.; Clem, P. G.; Fan, H. Stress-induced phase transformation and optical coupling of silver nanoparticle superlattices into mechanically stable nanowires. *Nat. Commun.* **2014**, *5*, 4179.
(70) Li, M.; Cushing, S. K.; Wu, N. Plasmon-enhanced optical sensors: a review. *Analyst* **2015**, *140*, 386−406.
(71) Sun, L.; Lin, H.; Kohlstedt, K. L.; Schatz, G. C.; Mirkin, C. A. Design principles for photonic crystals based on plasmonic nanoparticle superlattices. *Proc. Natl. Acad. Sci. U.S.A.* **2018**, *115*, 7242−7247.
(72) Jung, K.; Hahn, J.; In, S.; Bae, Y.; Lee, H.; Pikhitsa, P. V.; Ahn, K.; Ha, K.; Lee, J. K.; Park, N. Hotspot-engineered 3D multipetal flower assemblies for surface-enhanced Raman spectroscopy. *Adv. Mater.* **2014**, *26*, 5924−5929.
(73) Liu, H.; Yang, Z.; Meng, L.; Sun, Y.; Wang, J.; Yang, L.; Liu, J.; Tian, Z. Three-dimensional and time-ordered surface-enhanced Raman scattering hotspot matrix. *J. Am. Chem. Soc.* **2014**, *136*, 5332−5341.
(74) Wang, Y.; Yang, X.; Liu, T.; Li, Z.; Leskauskas, D.; Liu, G.; Matson, J. B. Molecular-level control over plasmonic properties in silver nanoparticle/self-assembling peptide hybrids. *J. Am. Chem. Soc.* **2020**, *142*, 9158−9162.
(75) Brust, M.; Fink, J.; Bethell, D.; Schiffrin, D. J.; Kiely, C. Synthesis and reactions of functionalised gold nanoparticles. *J. Chem. Soc., Chem. Commun.* **1995**, *16*, 1655−1656.
(76) Huh, J.; Ginzburg, V. V.; Balazs, A. C. Thermodynamic behavior of particle/diblock copolymer mixtures: Simulation and theory. *Macromolecules* **2000**, *33*, 8085−8096.
(77) Kao, J.; Xu, T. Nanoparticle assemblies in supramolecular nanocomposite thin films: concentration dependence. *J. Am. Chem. Soc.* **2015**, *137*, 6356−6365.
(78) Yeh, S. W.; Wu, T. L.; Wei, K. H.; Sun, Y. S.; Liang, K. S. Effect of incorporated CdS nanoparticles on the crystallinity and

https://doi.org/10.1021/jacs.3c10297
J. Am. Chem. Soc. XXXX, XXX, XXX−XXX

morphology of poly (styrene-*b*-ethylene oxide) diblock copolymers. *J. Polym. Sci., Part B: Polym. Phys.* **2005**, *43*, 1220−1229.
(79) Yeh, S.-W.; Wei, K.-H.; Sun, Y.-S.; Jeng, U.-S.; Liang, K. S. CdS nanoparticles induce a morphological transformation of poly (styrene-*b*-4-vinylpyridine) from hexagonally packed cylinders to a lamellar structure. *Macromolecules* **2005**, *38*, 6559−6565.

https://doi.org/10.1021/jacs.3c10297
J. Am. Chem. Soc. XXXX, XXX, XXX−XXX